ACS NANO
Cite This: ACS Nano 2019, 13, 5103−5111
www.acsnano.org

ARTICLE

Degenerately Doped Transition Metal Dichalcogenides as Ohmic Homojunction Contacts to Transition Metal Dichalcogenide Semiconductors

Zhibin Gao,[†,‡] Zhixian Zhou,[¶] and David Tománek*,[†,§]

[†]Physics and Astronomy Department, Michigan State University, East Lansing, Michigan 48824, United States

[‡]Center for Phononics and Thermal Energy Science, School of Physics Science and Engineering, Tongji University, 200092 Shanghai, People's Republic of China

[¶]Physics and Astronomy Department, Wayne State University, Detroit, Michigan 48201, United States

[§]Mandelstam Institute for Theoretical Physics and School of Physics, University of the Witwatersrand, 2050 Johannesburg, South Africa

Supporting Information

ABSTRACT: **In search of an improved strategy to form low-resistance contacts to MoS_2 and related semiconducting transition metal dichalcogenides, we use *ab initio* density functional electronic structure calculations in order to determine the equilibrium geometry and electronic structure of MoO_3/MoS_2 and MoO_2/MoS_2 bilayers. Our results indicate that, besides a rigid band shift associated with charge transfer, the presence of molybdenum oxide modifies the electronic structure of MoS_2 very little. We find that the charge transfer in the bilayer provides a sufficient degree of hole doping to MoS_2, resulting in a highly transparent contact region.**

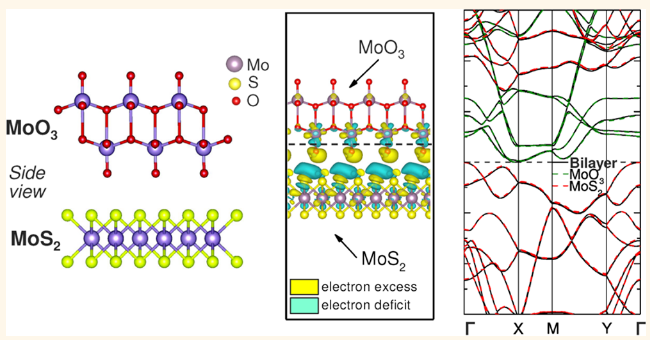

KEYWORDS: *transition metal dichalcogenides, contacts, ab initio calculations, electronic structure, charge transfer, doping, band offset*

One of the key challenges in 2D semiconductor physics is finding better ways to inject charge carriers through transparent, ohmic contacts[1−3] in order to reduce power dissipation and increase carrier mobility.[4,5] This problem does not occur in 3D semiconductors, where degenerate doping, resulting in transparent contacts to metal electrodes, is achieved by ion implantation.[6] That approach is not practical in atomically thin 2D layers, since bombardment by ions with a finite penetration depth would not only implant but also knock out atoms from the channel.[7] Several alternative approaches have been explored in the past. The most common among these is doping by elemental substitution[8−10] and by surface charge transfer.[7,11,12] Doping the entire structure does improve charge injection in the contact region, but also turns the channel metallic, reducing its switching capability.[13] Significant local doping by surface charge transfer may also be achieved using adsorbed molecules, but typically suffers from lack of chemical and thermal stability. Substitutional doping yields a stable structure, but cannot be strictly limited to the contact regions only. It generally causes structural changes and introduces scattering centers in the 2D channel, thus degrading its transport properties. Direct local contact between a 2D semiconductor and a metal with a favorable work function appears attractive, but typically results in a strong hybridization at the interface, causing the formation of midgap states and Fermi level pinning.[3,14−17] One way to reduce these negative side effects of a metal contact is to insert an ultrathin insulating layer such as h-BN or MgO in-between the semiconducting channel and the metal.[18−20] This approach favorably modifies the work function of the metal while reducing the net charge transfer between the contact metal and the channel, suppressing the formation of interlayer gap states and Fermi level pinning. The drawback of this approach is widening the vertical tunnel barrier between the contact metal and the channel. Whereas formation of midgap states can be

Received: October 25, 2018
Accepted: April 30, 2019
Published: April 30, 2019

DOI: 10.1021/acsnano.8b08190
ACS Nano 2019, 13, 5103−5111

avoided when using substitutionally heavily doped or metallic 2D transition metal dichalcogenides in van der Waals contact with the channel,[10,21] the vertical tunnel barrier cannot be eliminated. An unusual way to optimize contacts to 2D semiconductors, which does not involve charge transfer to the channel, is by phase engineering.[22−24] In this approach, an in-layer homojunction is formed when locally converting the semiconducting 2H phase of the channel material such as MoS_2 to a metastable, metallic 1T phase. This approach is, however, restricted to selected materials, and the phase stability is limited. All of the above strategies have significant drawbacks, which make continuing the search for suitable alternatives highly desirable.

We propose a previously unexplored approach to achieve degenerate hole doping in a local region of a semiconducting MoS_2 channel that is placed in direct contact with electronegative materials such as MoO_3 or MoO_2 using van der Waals assembly. To prove the viability of this approach, we perform *ab initio* density functional calculations of the vertical heterostructure using density functional theory (DFT), which is known to describe charge distribution and doping correctly. We find that the charge transfer between the doping layer and the channel is significant and results in degenerate doping of the MoS_2 channel by the adjacent molybdenum oxide layer. With only negligible hybridization at the bilayer interface and its negative side effects, the dominant electronic structure change is a net charge transfer giving rise to an interface dipole, which causes a rigid shift[21] of the MoS_2 bands in the contact region and turns it metallic. In this case, no vertical tunnel barrier will form when the heavily doped and highly conducting contact region of the channel material is contacted by a metal on the side opposite the molybdenum oxide.

In common Si-based 3D semiconductor devices, charge transport is dominated by the intrinsic properties of the channel. Contacts do not play a significant role, since the contact region is degenerately doped by ion implantation, which allows for barrier-free charge injection from a metal electrode.[6] The device characteristics change significantly in low-dimensional semiconductors, where contacts play the dominant role due to significant Schottky barriers and an associated wide depletion region caused by insufficient screening. The key role of Schottky barriers in the contact region has been recognized early in 1D semiconducting carbon nanotubes with metal contacts,[25] with similar behavior extending to 2D semiconductors with metal contacts.[26] There, the contact resistance can be reduced, albeit not eliminated, by selecting contact metals with a work function aligned with the valence band maximum (VBM) or conduction band minimum (CBM), depending on the type of carriers to be injected.[14,27]

Our alternative approach is to create a homojunction between a doped and a pristine segment of a 2D semiconductor such as MoS_2. Key to this approach is the use of van der Waals assembly to contact the channel by a highly electronegative material that locally provides degenerate hole doping. The material of choice in this study is MoO_3 with a very high work function[28] of 6.7 eV. This material has emerged as a promising surface acceptor material for a wide variety of systems including diamond thin films, graphene, and transition metal dichalcogenides (TMDs).[29−32] Because the CBM of MoO_3 lies below the VBM of most semiconductors including TMDs, molybdenum oxide is a viable candidate to provide degenerate doping to 2D semiconductors.

RESULTS

MoS_2 in Contact with MoO_3. The structure of isolated MoO_3 and MoS_2 monolayers, as well as that of the bilayer, is shown in Figure 1. The Bravais lattice of MoO_3 has a rectangular unit cell containing 2 Mo and 6 O atoms with a_1 = 3.71 Å and a_2 = 3.95 Å. The calculated cohesive energy per formula unit of a free-standing MoO_3 monolayer is E_{coh} = 24.62 eV with respect to isolated atoms.

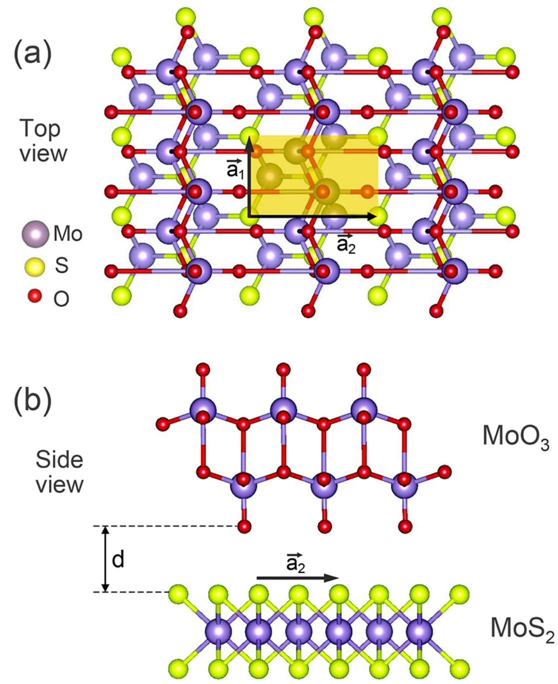

Figure 1. Ball-and-stick model of the MoO_3/MoS_2 bilayer in (a) top view and (b) side view. The unit cell is indicated by yellow shading in (a). $\vec{a}_1$ and $\vec{a}_2$ are the lattice vectors spanning the 2D lattice, and *d* is the interlayer distance.

MoS_2 forms a triangular lattice with the lattice constant a = 3.18 Å. The corresponding lattice constants of a conventional rectangular unit cell containing 2 Mo and 4 S atoms, useful when discussing epitaxy with MoO_3, are a_1 = 3.18 Å and a_2 = 5.51 Å. The calculated cohesive energy per formula unit of free-standing MoS_2 is E_{coh} = 16.37 eV with respect to isolated atoms.

Since the computational approach to investigate infinite structures requires a periodic array of identical unit cells and since the MoO_3 and the MoS_2 layers are incommensurate, we need to enforce commensurability by subjecting the individual layers to in-layer strain at some energy cost. To obtain quantitative understanding of the effect of strain on our results, we distinguished the smaller supercell A containing 4 Mo, 6 O, and 4 S atoms, shown in Figure 1(a), from the larger supercell B, which contains 44 Mo, 72 O, and 40 S atoms. Both supercells are shown in the Supporting Information. The primary reason to consider the smaller supercell A, which is highly strained, is to obtain an intuitive understanding of the physics. The larger supercell B is less strained and expected to provide a better quantitative agreement with the real system.

The strain energy in stretched and compressed MoO_3 and MoS_2 monolayers as well as in the bilayer is shown in Figure 2. The deformation energies ΔE, shown as a function of the lattice constants in Figure 2(a−e), allow judging the in-plane

DOI: 10.1021/acsnano.8b08190
ACS Nano 2019, 13, 5103−5111

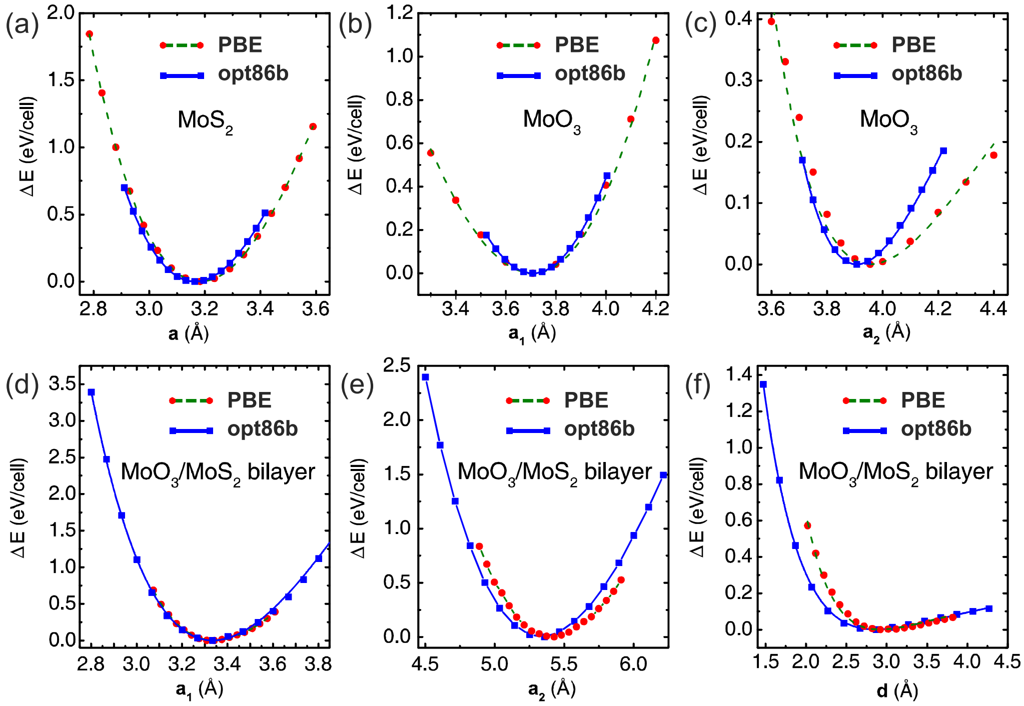

Figure 2. Energy change ΔE per unit cell as a function of the lattice parameters. Monolayer results are presented for (a) MoS_2 with 3-fold symmetry and lattice constant a and (b, c) MoO_3 with lattice constants a_1 and a_2. The unit cells we consider contain 3 atoms in (a) and 8 atoms in (b) and (c). MoO_3/MoS_2 bilayer results representing 14-atom unit cells show ΔE as a function of (d) a_1, (e) a_2, and (f) the interlayer distance d. The dashed lines in (a)−(d) and (f) are fits by the Morse potential. The dashed line in (e) is a guide to the eye. The legend in the panels specifies the symbols and line types for results based on DFT-PBE and also the DFT-optB86b-vdW functional, which specifically considers the van der Waals interaction.

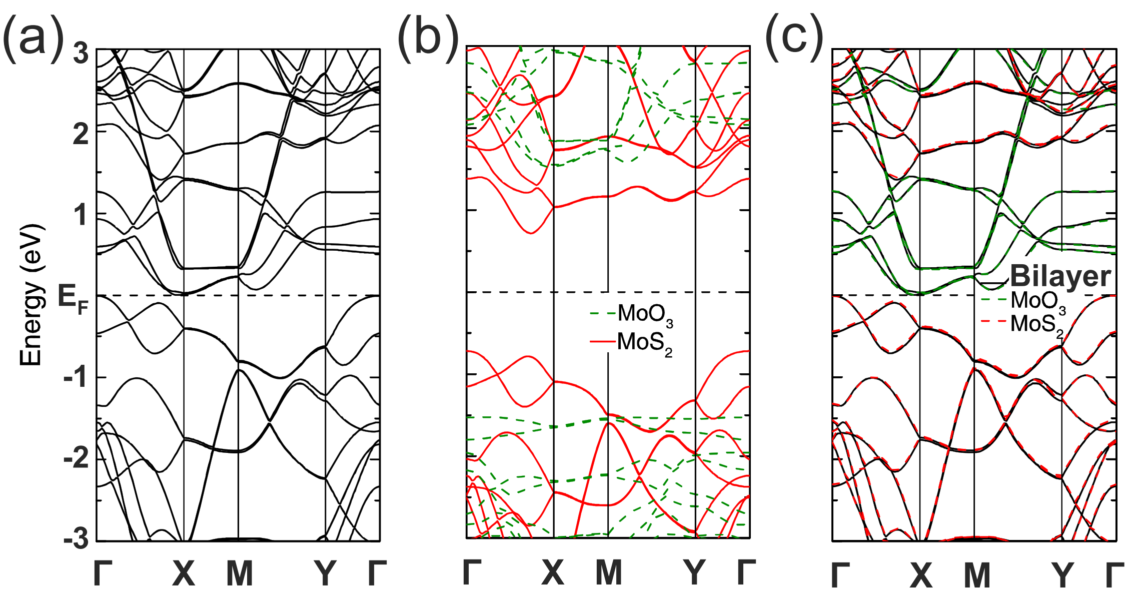

Figure 3. (a) Electronic band structure of a MoO_3/MoS_2 bilayer with supercell A. (b) Superposition of the electronic band structure of isolated monolayers of MoS_2 (solid red lines) and MoO_3 (dashed green lines). (c) Superposition of the MoS_2 bands in panel (b), shifted rigidly up by 0.711 eV, and the MoO_3 bands, shifted rigidly down by 1.523 eV. The combined band structure in (c) is superposed to that of the MoO_3/MoS_2 bilayer in panel (a).

compressibility of the MoO_3/MoS_2 bilayer and its components. The interlayer interaction energy in the bilayer system with supercell A, shown in Figure 2(f), has been fitted by the Morse potential $\Delta E = E_0[1 - \exp(\xi[d - d_0])]$.

We find results based on DFT-PBE to be in very good agreement with those based on the DFT-optB86b-vdW functional. This indicates that the role of van der Waals interactions, which are specifically addressed in the latter functional, is only secondary. Since our results for both supercells indicate a significant charge redistribution within the vertical heterojunction, the role of the Coulomb attraction between adjacent MoO_3 and MoS_2 layers is more significant. We note that Coulomb interaction is described adequately by the DFT formalism.

DOI: 10.1021/acsnano.8b08190
ACS Nano 2019, 13, 5103−5111

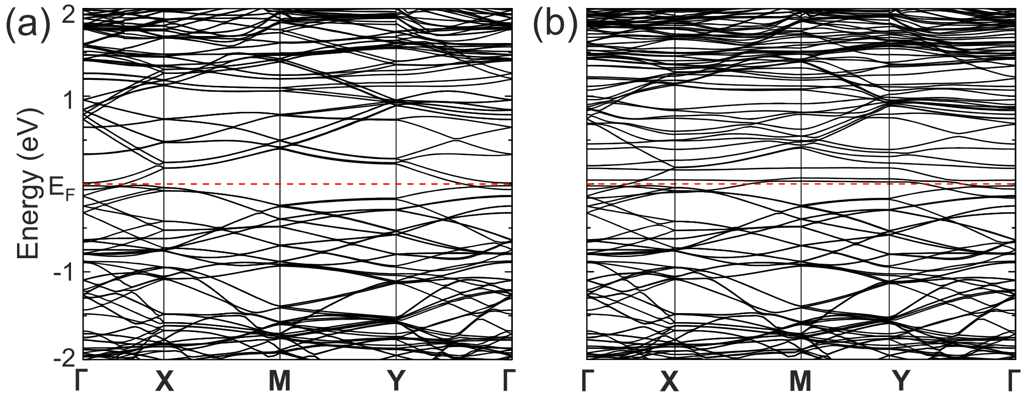

Figure 4. Electronic band structure of a MoO_{3-x}/MoS_2 bilayer based on DFT-PBE and represented by supercell B containing 156 atomic sites in total. Results for a defect-free system ($x = 0$) (a) are compared to those for a defective system ($x > 0$) with one oxygen vacancy in each unit cell (b). The Fermi level is indicated by the red dashed line.

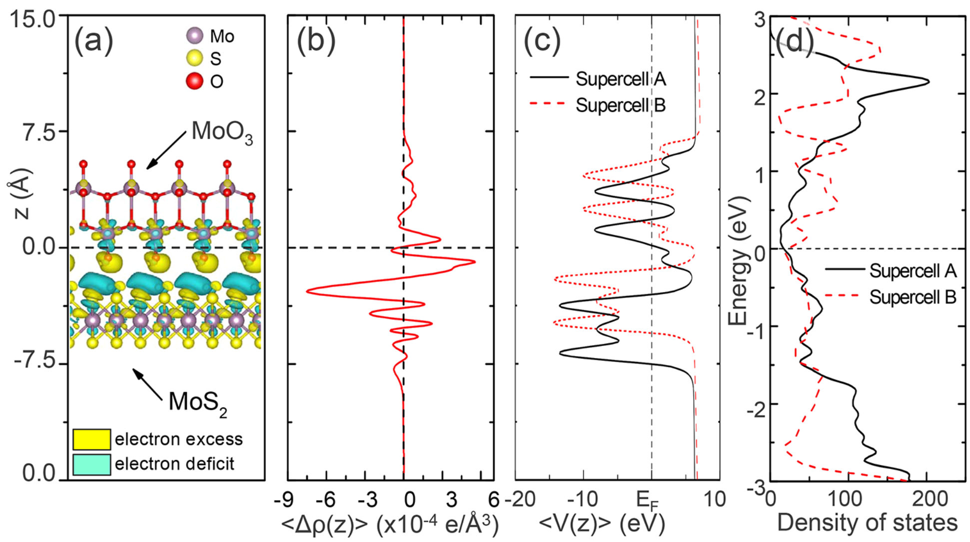

Figure 5. Electronic structure changes associated with assembling the MoO_3/MoS_2 bilayer from isolated monolayers. (a) Charge density difference $\Delta\rho = \rho(MoO_3/MoS_2) - \rho(MoO_3) - \rho(MoS_2)$. $\Delta\rho$ is shown by isosurfaces bounding regions of electron excess at $+1.0 \times 10^{-3}$ e/Å^3 (yellow) and electron deficiency at -1.0×10^{-3} e/Å^3 (blue). (b) $\langle\Delta\rho(z)\rangle$ averaged across the x−y plane of the layers. The black solid reference line is a guide to the eye. z indicates the position of the plane. (c) Electrostatic potential $\langle V(z)\rangle$ in the bilayer, averaged across the x−y plane, with z denoting the position of the plane. (d) Density of states of the bilayer, convoluted by a Gaussian with a full-width at half-maximum of 0.1 eV. (c) and (d) display results for supercell A (solid black line) and supercell B (dashed red line), defined in the text.

The relaxed geometry of the bilayer structure with the rectangular supercell A is characterized by the lattice constants a_1 = 3.34 Å and a_2 = 5.42 Å and the unit cell area A_A = 18.11 Å^2. We note that the optimum values of a_1 and a_2 in the bilayer lie in-between the values of the isolated monolayers. In the MoO_3 layer within the relaxed bilayer with supercell A, a_1 is compressed by 9.8% and a_2 is stretched by 37.0% at the energy cost of 5.5 eV/nm^2. In the MoS_2 layer in the same geometry, a_1 is stretched by 5.1% and a_2 is compressed by 1.6% at the energy cost of 0.9 eV/nm^2. The attractive interaction energy between the strained layers amounts to 0.1 eV/nm^2.

The relaxed geometry of the bilayer structure with the larger rectangular supercell B is characterized by the lattice constants a_1 = 15.87 Å and a_2 = 11.07 Å and the unit cell area A_B = 175.72 Å^2. We note again that the optimum a_1 and a_2 values in the bilayer are in-between the values of the isolated monolayers. The relative deformations and the deformation energies are much smaller in the larger supercell B. In the MoO_3 layer within the relaxed bilayer with supercell B, a_1 is stretched by 7.0% and a_2 is compressed by 6.7% at the energy cost of 0.3 eV/nm^2. In the MoS_2 layer within the same relaxed bilayer geometry, a_1 is compressed by 0.2% and a_2 is stretched by 0.5% at the energy cost of 0.6 eV/nm^2. The attractive interaction energy between the strained layers in the bilayer amounts to 0.7 eV/nm^2, nearly compensating for the deformation energy of the individual layers.

To obtain a basic understanding of what is happening in the system electronically, we first consider the smaller supercell A of the MoO_3/MoS_2 bilayer. The electronic band structure based on DFT-PBE Kohn−Sham eigenvalues, shown in Figure 3(a), suggests that the system is semimetallic. A superposition of electronic band structures of isolated MoO_3 and MoS_2 monolayers, constrained to their respective structure in the bilayer, is shown in Figure 3(b), with the Fermi levels aligned at midgap. In view of the fact that fundamental gaps are typically underestimated in the Kohn−Sham DFT-PBE spectrum, we expect that the MoO_3/MoS_2 bilayer with supercell A, as well as the MoO_3 and MoS_2 monolayers, should be semiconducting. This expectation is confirmed in the corresponding band structure and density of states

DOI: 10.1021/acsnano.8b08190
ACS Nano 2019, 13, 5103−5111

obtained using the hybrid DFT-HSE06 exchange−correlation functional, which is presented in the Supporting Information. Kohn−Sham spectra based on DFT-HSE06 typically have wider fundamental band gaps that agree better with observed electronic spectra than spectra based on DFT-PBE.

To inspect the level of hybridization at the interface, we superposed the DFT-PBE band structure of the bilayer with the bands of an isolated MoS_2 monolayer, shifted rigidly up by 0.711 eV, and a MoO_3 monolayer, shifted rigidly down by 1.523 eV. Comparing the band superposition with the bilayer band structure in Figure 3(c), we find only a minimum degree of hybridization between the individual layers. The same small degree of hybridization also occurs in DFT-HSE06 calculations. Similar to DFT-PBE results, the DFT-HSE06 band structure of the bilayer is represented well by a superposition of MoS_2 monolayer bands, shifted rigidly up by 0.660 eV, and MoO_3 monolayer bands, shifted rigidly down by 2.461 eV.

In truth, the above semiconducting behavior is not intrinsic to the MoO_3/MoS_2 bilayer, but rather linked to using the small supercell A. DFT-PBE band structure results for the bilayer represented by the much larger and more adequate supercell B, presented in Figure 4(a), indicate a much higher degree of metallicity at the Fermi level. In realistic MoO_{3-x} systems, there are nonstoichiometric composition variations with oxygen vacancies.[31,33] As shown in Figure 4(b), such oxygen vacancies always cause partly filled bands associated with metallic behavior.

The charge redistribution in the bilayer is shown in Figure 5. The net charge transferred from the MoS_2 to the MoO_3 layer is $\Delta\rho_{2D} = 2.0 \times 10^{13}$ e/cm^2 in the bilayer with the smaller supercell A and $\Delta\rho_{2D} = 4.5 \times 10^{13}$ e/cm^2 in the bilayer with the larger supercell B. When divided by the thickness $t \approx 0.4$ nm of the MoS_2 channel, the charge transfer density ranges from $\Delta\rho = 5 \times 10^{20}$ to 1×10^{21} e/cm^3. This is high enough and considered degenerate doping, since E_F has been moved into the valence band. Having achieved degenerate doping in the contact region of the bilayer, the tunnel barrier to a metal contact at the side opposite the doping layer should also be negligibly small and of no consequence.

MoS_2 in Contact with MoO_2. As mentioned before, experimental studies report nonstoichiometric variations of MoO_{3-x} with oxygen vacancies and amorphous structure,[31,33] which cannot be modeled as periodic structures. As a step in the direction of molybdenum oxide with a lower oxygen concentration, we consider instead the MoO_2 stoichiometry. MoO_2 has been discussed theoretically and found to form a stable honeycomb lattice,[34] different from the MoO_3 lattice with a rectangular unit cell. Since MoO_2 shares the same 6-fold symmetry with MoS_2, we have considered this system as a potential alternative to MoO_3 in hole-doping MoS_2.

The structure of the isolated MoO_2 and MoS_2 monolayers and the bilayer structure are shown in Figure 6. Unlike MoO_3, MoO_2 forms a honeycomb lattice with the lattice constant a = 2.83 Å. The calculated cohesive energy per formula unit of a free-standing MoO_2 monolayer is E_{coh} = 19.65 eV with respect to isolated atoms.

We describe the MoO_2/MoS_2 bilayer by an epitaxial triangular Bravais lattice with a basis and one formula unit per unit cell. The optimum lattice constant is $a = |\vec{a}_1| = |\vec{a}_2| =$ 2.99 Å, and the unit cell area is A = 7.72 Å^2. We note that the optimum value of a in the bilayer is in-between the values of the isolated monolayers. In the MoO_2 layer, a is stretched by 5.5% at the energy cost of 5.2 eV/nm^2. In the MoS_2 layer, a is compressed by 6.1% at the energy cost of 4.5 eV/nm^2. The attractive interaction energy between the strained layers amounts to 0.1 eV/nm^2.

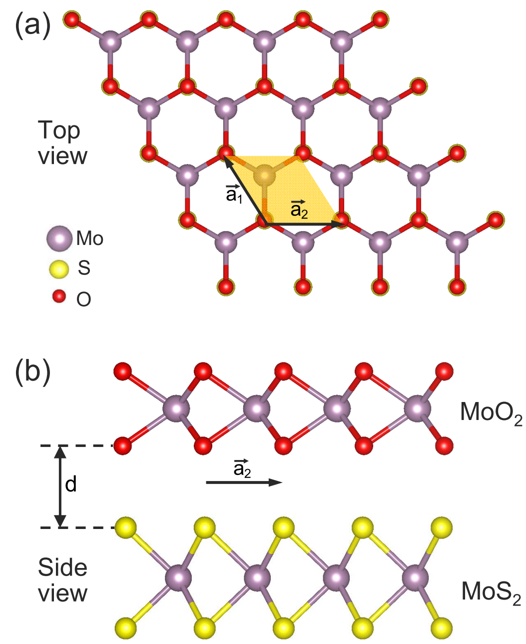

Figure 6. Ball-and-stick model of the MoO_2/MoS_2 bilayer in (a) top view and (b) side view. The unit cell is indicated by yellow shading in (a). $\vec{a}_1$ and $\vec{a}_2$ are the lattice vectors spanning the 2D lattice, and d is the interlayer distance.

Similar to MoO_3 interacting with MoS_2, also interacting monolayers of MoO_2 and MoS_2 need to be strained to form a commensurate structure. The unit cell of the bilayer, shown in Figure 6(b), contains 2 Mo, 2 S, and 2 O atoms. The strain energy in stretched and compressed MoO_2 and MoS_2 monolayers as well as the bilayer is shown in Figure 7. Also in this system, we find results based on DFT-PBE to be in very good agreement with those based on the DFT-optB86b-vdW functional. This indicates that van der Waals interactions, which are specifically considered in the latter functional, play only a secondary role.

The electronic band structure of the MoO_2/MoS_2 bilayer, shown in Figure 8(a), indicates that the system is metallic as hoped for. A superposition of electronic band structures of isolated MoO_2 and MoS_2 monolayers, constrained to their respective structure in the bilayer, is shown in Figure 8(b), with the Fermi levels of the individual layers aligned. In contrast to the MoS_2 channel, our results suggest that MoO_2 should be metallic. In view of the fact that DFT-PBE calculations typically underestimate band gaps, we realistically expect MoO_2 to be a semiconductor with a narrow, indirect band gap instead. This is confirmed by DFT-HSE06 band structure and density of states results, presented in the Supporting Information, which indicate a 0.5 eV wide indirect band gap in an isolated MoO_2 monolayer. To inspect the level of hybridization at the MoO_2/MoS_2 interface, we superposed the band structure of the bilayer with the bands of the MoS_2 monolayer, shifted rigidly up by 0.768 eV, and the unshifted bands of the MoO_2 monolayer. Comparing the band superposition with the bilayer band structure in Figure 8(c), we find only a minimum degree of hybridization in the system. The same low degree of hybridization, but a significant charge

DOI: 10.1021/acsnano.8b08190
ACS Nano 2019, 13, 5103−5111

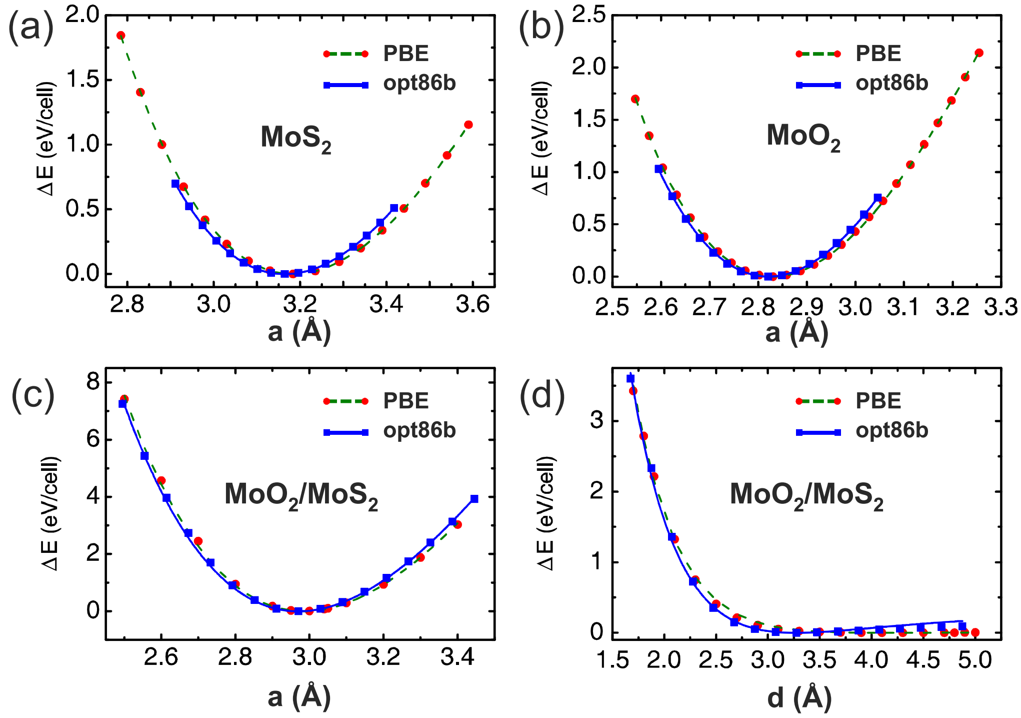

Figure 7. Energy change **Δ*E*** per unit cell as a function of the lattice constant *a* in monolayers of (a) MoS_2 and (b) MoO_2. **Δ*E*** per unit cell in MoO_2/MoS_2 bilayers as a function of (c) the lattice constant *a* and (d) the interlayer distance *d*. The dashed lines are fits by the Morse potential. The legend in the panels specifies the symbols and line types for results based on DFT-PBE and for those based on the DFT-optB86b-vdW functional, which specifically considers the van der Waals interaction.

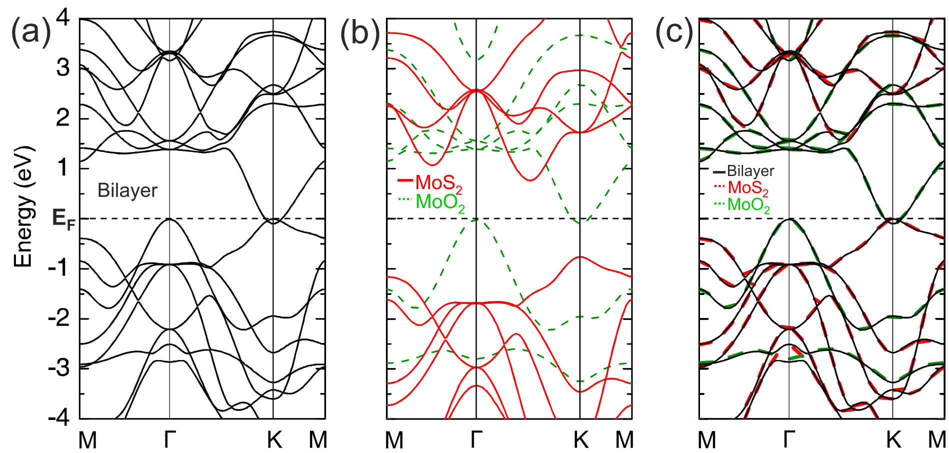

Figure 8. (a) Electronic band structure of a MoO_2/MoS_2 bilayer. (b) Superposition of the electronic band structure of isolated monolayers of MoS_2 (solid red lines) and MoO_2 (dashed green lines). (c) Superposition of the MoS_2 bands in panel (b), shifted rigidly up by 0.768 eV, and the unshifted MoO_2 bands. The combined band structure in (c) is superposed to that of the MoO_2/MoS_2 bilayer in panel (a).

transfer from MoS_2 to MoO_2 causing a net metallic behavior of the bilayer, is also found in corresponding DFT-HSE06 band structure results presented in the Supporting Information.

The charge redistribution in the bilayer is shown in Figure 9. The net charge transferred from the MoS_2 to the MoO_2 layer is $\Delta\rho_{2D} = 1.7 \times 10^{13}$ e/cm^2 in the bilayer. When divided by the thickness $t \approx 0.4$ nm of the MoS_2 channel, the charge transfer density amounts to $\Delta\rho = 4 \times 10^{20}$ e/cm^3, slightly lower than in the MoO_3/MoS_2 bilayer. This doping level is still considered to be degenerate, since E_F has been moved into the valence band of the channel. With degenerate doping in the contact region of the bilayer, the tunnel barrier to a metal contact on the side opposite the doping layer should again be negligibly small and of no consequence.

DISCUSSION

As expected in the outset, our numerical results based on a Bader charge analysis indicate a significant charge transfer between adjacent MoO_{3-x} and MoS_2 layers in the bilayer geometry. To validate the amount of charge transferred between the layers, we compared the charge density difference $\Delta\rho_{2D}$ based on the current DFT-PBE nonlocal exchange correlation functional to those based on the local DFT-LDA functional. The specific values for $\Delta\rho_{2D}$ in MoO_3/MoS_2 are 5.55×10^{13} e/cm^2 (LDA for supercell B), 4.49×10^{13} e/cm^2

DOI: 10.1021/acsnano.8b08190
ACS Nano 2019, 13, 5103−5111

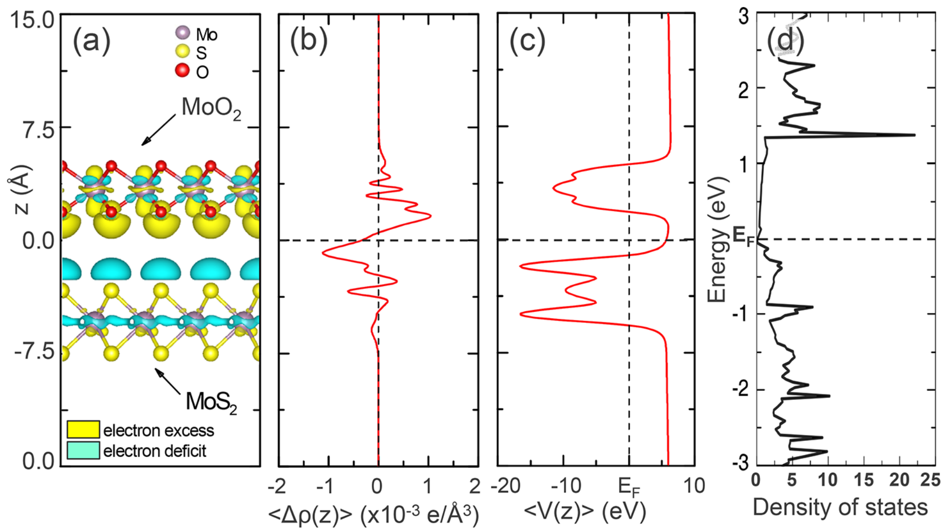

Figure 9. Electronic structure changes associated with assembling the MoO_2/MoS_2 bilayer from isolated monolayers. (a) Charge density difference $\Delta\rho = \rho(MoO_2/MoS_2) - \rho(MoO_2) - \rho(MoS_2)$. $\Delta\rho$ is shown by isosurfaces bounding regions of electron excess at $+1.0 \times 10^{-3}$ e/Å^3 (yellow) and electron deficiency at -1.0×10^{-3} e/Å^3 (blue). (b) $\langle\Delta\rho(z)\rangle$ averaged across the $x-y$ plane of the layers. The black solid reference line is a guide to the eye, and z indicates the position of the plane. (c) Electrostatic potential $\langle V(z)\rangle$ in the bilayer, averaged across the $x-y$ plane, with z denoting the position of the plane. (d) Density of states of the bilayer, convoluted by a Gaussian with a full-width at half-maximum of 0.1 eV.

(PBE for supercell B), 2.09×10^{13} e/cm^2 (LDA for supercell A), and 1.97×10^{13} e/cm^2 (PBE for supercell A). The corresponding values for $\Delta\rho_{2D}$ in MoO_2/MoS_2 are 1.80×10^{13} e/cm^2 (LDA) and 1.67×10^{13} e/cm^2 (PBE). These results clearly indicate that the effect of the exchange−correlation functional on the charge transfer is very small. Since the treatment of exchange and correlation in the hybrid DFT-HSE06 functional with a slowly decaying Fock exchange is fundamentally different from the more localized form in DFT-LDA and DFT-PBE functionals,[35,36] the DFT-HSE06 functional does not provide a simple way for a Bader charge decomposition and is not used for this purpose in our study.

In order to eliminate the tunnel barrier between a contact metal and a 2D semiconductor such as MoS_2, we have proposed a way to locally hole dope the channel using a stable 2D material. To achieve this objective without causing hybridization and the emergence of midgap states, we chose the highly electronegative 2D semiconductor MoO_3 or, alternatively, MoO_2. Our results confirm the expectation that the band structure in the contact region closely resembles the superposition of energetically shifted bands of MoS_2 and MoO_3 or MoO_2. We observed degenerate hole doping of the channel in contact with electronegative MoO_3 and MoO_2 layers. The rigid band shift in the doped contact region has an important side effect, namely, a rigid shift of the channel bands in the doped with respect to the undoped channel region. This is of no consequence for the vertical tunnel barrier in the contact region, which will become negligibly small if the channel in the conducting contact region is contacted on the side opposite the molybdenum oxide by a metal. In this case, we may say that we have reached the main objective of our study, which was to optimize the metal−channel contact, using our approach.

However, another challenge has emerged that had been overlooked so far to a large degree. The rigid shift of the channel bands in the contact region causes a band offset with respect to the undoped channel region, causing the formation of an in-plane Schottky barrier. Since screening in a 2D system is much lower than in conventional 3D systems, the resulting depletion region will be larger.[26] The in-layer Schottky barriers have to be considered seriously, since their effect on carrier injection may be larger than that of the vertical tunnel barriers. In that case, this lateral Schottky barrier may dominate the contact transparency.

In principle, the band offset and the associated Schottky barrier could be reduced by replacing the semiconducting channel material outside the contact region by a different, isoelectronic material. In the specific case of p-doped MoS_2, using materials with their VBM aligned with or even higher than the shifted VBM of the channel in the contact region will eliminate such a lateral Schottky barrier and thus improve charge injection. Potential candidates for in-layer contacts with the heavily p-doped MoS_2 segment are WSe_2 and $MoTe_2$ as the channel material.[37] Formation of such contacts by epitaxial growth of monolayer WSe_2−MoS_2 lateral junctions with an atomically sharp interface has recently been demonstrated.[38] As an alternative, isoelectronic alloying in the channel region may be used.[39] Whether the Schottky barrier is reduced by a lateral 2D/2D junction of different materials or by isoelectronic doping, either approach will create additional interface or impurity scattering centers.

CONCLUSIONS

We have proposed an improved strategy to form low-resistance contacts to MoS_2 and related semiconducting transition metal dichalcogenides by local degenerate hole doping in the contact region, where the atomically thin 2D channel material is in direct contact with an electronegative material such as MoO_3 or MoO_2. In contrast to metal contacts that are separate from the undoped 2D channel material, the homojunction in our study is between undoped and heavily doped regions of the same 2D material. To check the viability of this approach, we have determined the equilibrium geometry and electronic structure of MoO_3/MoS_2 and MoO_2/MoS_2 bilayers and their monolayer components using *ab initio* density functional calculations. Our results indicate that, besides a rigid band shift

DOI: 10.1021/acsnano.8b08190
ACS Nano 2019, 13, 5103−5111

associated with charge transfer, the presence of molybdenum oxide modifies the electronic structure of MoS_2 very little, thus avoiding the formation of midgap states. We found that the charge transfer in the bilayer provides a sufficient degree of hole doping to MoS_2 to render the contact region metallic. A highly transparent contact will thus be formed by sandwiching the semiconducting 2D MoS_2 channel material in-between Mo oxide and a metal.

METHODS

We have studied the electronic structure, the equilibrium geometry, and structural stability of MoO_3 and MoO_2 interacting with MoS_2 using *ab initio* DFT as implemented in the VASP code.[40−42] We represented these 2D structures by a periodic array of layers separated by a vacuum region in excess of 20 Å. We used projector-augmented-wave (PAW) pseudopotentials[43,44] and the Perdew−Burke−Ernzerhof (PBE)[45] and the optB86b-vdW[46,47] exchange−correlation functionals. Since the fundamental band gap is usually underestimated in DFT-PBE calculations, we have resorted to the HSE06[35,36] hybrid exchange−correlation functional, as implemented in the VASP[40−42,44] code, to get a different (possibly superior) description of the band structure. We used the default mixing parameter value $\alpha = 0.25$ in these studies. The Brillouin zone of the conventional unit cell of the 2D structures has been sampled by a uniform *k*-point grid.[48] The specific sampling we used was 15 × 15 for MoS_2, MoO_3, and MoO_2 monolayers as well as the MoO_2/MoS_2 bilayer, 9 × 9 for the MoO_3/MoS_2 bilayer with the supercell A containing 14 atoms, and 2 × 2 for the MoO_3/MoS_2 bilayer with supercell B containing 156 atoms. We used 550 eV as the electronic kinetic energy cutoff for the plane-wave basis and a total energy difference between subsequent self-consistency iterations below 10^{-5} eV/atom as the criterion for reaching self-consistency. All geometries have been optimized using the conjugate-gradient method,[49] until none of the residual Hellmann−Feynman forces exceeded 10^{-3} eV/Å. The maximum force criterion has been relaxed to 10^{-2} eV/Å in the optimization of the MoO_3/MoS_2 bilayer with the large supercell B containing 156 atoms.

ASSOCIATED CONTENT

Supporting Information

The Supporting Information is available free of charge on the ACS Publications website at DOI: 10.1021/acsnano.8b08190.

Supercells used to represent the incommensurate MoO_3/MoS_2 bilayer; comparison between the electronic band structure and density of states of MoO_3/MoS_2 and MoO_2/MoS_2 obtained using the DFT-HSE06 and DFT-PBE exchange−correlation functionals (PDF)

AUTHOR INFORMATION

Corresponding Author

*E-mail: tomanek@pa.msu.edu.

ORCID

David Tománek: 0000-0003-1131-4788

Notes

The authors declare no competing financial interest.

ACKNOWLEDGMENTS

D.T. acknowledges partial support by the NSF/AFOSR EFRI 2-DARE grant number EFMA-1433459. Z.G. acknowledges financial support from the China Scholarship Council under grant number 201706260027 and the hospitality of Michigan State University. Z.Z. acknowledges partial support by NSF grant number DMR-1308436 and the WSU Presidential Research Enhancement Award. Z.G. acknowledges useful discussions with Jie Ren. Computational resources have been provided by the Michigan State University High Performance Computing Center.

REFERENCES

(1) Allain, A.; Kang, J.; Banerjee, K.; Kis, A. Electrical Contacts to Two-Dimensional Semiconductors. *Nat. Mater.* **2015**, *14*, 1195.

(2) Popov, I.; Seifert, G.; Tománek, D. Designing Electrical Contacts to MoS_2 Monolayers: A Computational Study. *Phys. Rev. Lett.* **2012**, *108*, 156802.

(3) Kang, J.; Liu, W.; Sarkar, D.; Jena, D.; Banerjee, K. Computational Study of Metal Contacts to Monolayer Transition-Metal Dichalcogenide Semiconductors. *Phys. Rev. X* **2014**, *4*, 031005.

(4) Lopez-Sanchez, O.; Lembke, D.; Kayci, M.; Radenovic, A.; Kis, A. Ultrasensitive Photodetectors Based on Monolayer MoS_2. *Nat. Nanotechnol.* **2013**, *8* (8), 497.

(5) Cui, X.; Lee, G.-H.; Kim, Y. D.; Arefe, G.; Huang, P. Y.; Lee, C.-H.; Chenet, D. A.; Zhang, X.; Wang, L.; Ye, F.; Pizzocchero, F.; Jessen, B. S.; Watanabe, K.; Taniguchi, T.; Muller, D. A.; Low, T.; Kim, P.; Hone, J. Multi-Terminal Transport Measurements of MoS_2 Using a van der Waals Heterostructure Device Platform. *Nat. Nanotechnol.* **2015**, *10*, 534.

(6) Yu, A. Y. C. Electron Tunneling and Contact Resistance of Metal-Silicon Contact Barriers. *Solid-State Electron.* **1970**, *13*, 239−247.

(7) Fang, H.; Tosun, M.; Seol, G.; Chang, T. C.; Takei, K.; Guo, J.; Javey, A. Degenerate *n*−doping of Few-Layer Transition Metal Dichalcogenides by Potassium. *Nano Lett.* **2013**, *13*, 1991−1995.

(8) Yang, L.; Majumdar, K.; Liu, H.; Du, Y.; Wu, H.; Hatzistergos, M.; Hung, P. Y.; Tieckelmann, R.; Tsai, W.; Hobbs, C.; Ye, P. D. Chloride Molecular Doping Technique on 2D Materials: WS_2 and MoS_2. *Nano Lett.* **2014**, *14*, 6275−6280.

(9) Suh, J.; Park, T.-E.; Lin, D.-Y.; Fu, D.; Park, J.; Jung, H. J.; Chen, Y.; Ko, C.; Jang, C.; Sun, Y.; Sinclair, R.; Chang, J.; Tongay, S.; Wu, J. Doping Against the Native Propensity of MoS_2: Degenerate Hole Doping by Cation Substitution. *Nano Lett.* **2014**, *14*, 6976−6982.

(10) Chuang, H.-J.; Chamlagain, B.; Koehler, M.; Perera, M. M.; Yan, J.; Mandrus, D.; Tománek, D.; Zhou, Z. Low-Resistance 2D/2D Ohmic Contacts: A Universal Approach to High-Performance WSe_2, MoS_2, and $MoSe_2$ Transistors. *Nano Lett.* **2016**, *16*, 1896−1902.

(11) Fang, H.; Chuang, S.; Chang, T. C.; Takei, K.; Takahashi, T.; Javey, A. High-Performance Single Layered WSe_2 *p*−FETs with Chemically Doped Contacts. *Nano Lett.* **2012**, *12*, 3788−3792.

(12) Kiriya, D.; Tosun, M.; Zhao, P.; Kang, J. S.; Javey, A. Air-Stable Surface Charge Transfer Doping of MoS_2 by Benzyl Viologen. *J. Am. Chem. Soc.* **2014**, *136*, 7853−7856.

(13) Cai, L.; McClellan, C. J.; Koh, A. L.; Li, H.; Yalon, E.; Pop, E.; Zheng, X. Rapid Flame Synthesis of Atomically Thin MoO_3 down to Monolayer Thickness for Effective Hole Doping of WSe_2. *Nano Lett.* **2017**, *17*, 3854−3861.

(14) Tománek, D. Interfacing Graphene and Related 2D Materials with the 3D World. *J. Phys.: Condens. Matter* **2015**, *27*, 133203.

(15) Chen, W.; Santos, E. J.; Zhu, W.; Kaxiras, E.; Zhang, Z. Tuning the Electronic and Chemical Properties of Monolayer MoS_2 Adsorbed on Transition Metal Substrates. *Nano Lett.* **2013**, *13*, 509−514.

(16) Gong, C.; Colombo, L.; Wallace, R. M.; Cho, K. The Unusual Mechanism of Partial Fermi Level Pinning at Metal-MoS_2 Interfaces. *Nano Lett.* **2014**, *14*, 1714−1720.

(17) Movva, H. C.; Rai, A.; Kang, S.; Kim, K.; Fallahazad, B.; Taniguchi, T.; Watanabe, K.; Tutuc, E.; Banerjee, S. K. High-Mobility Holes in Dual-Gated WSe_2 Field-effect Transistors. *ACS Nano* **2015**, *9*, 10402−10410.

(18) Chen, J.-R.; Odenthal, P. M.; Swartz, A. G.; Floyd, G. C.; Wen, H.; Luo, K. Y.; Kawakami, R. K. Control of Schottky Barriers in Single Layer MoS_2 Transistors with Ferromagnetic Contacts. *Nano Lett.* **2013**, *13*, 3106−3110.

(19) Wang, J.; Yao, Q.; Huang, C.-W.; Zou, X.; Liao, L.; Chen, S.; Fan, Z.; Zhang, K.; Wu, W.; Xiao, X.; Jiang, C.; Wu, W.-W. High

DOI: 10.1021/acsnano.8b08190
ACS Nano 2019, 13, 5103−5111

Mobility MoS_2 Transistor with Low Schottky Barrier Contact by Using Atomic Thick *h*−BN as a Tunneling Layer. *Adv. Mater.* **2016**, *28*, 8302−8308.

(20) Cui, X.; Shih, E.-M.; Jauregui, L. A.; Chae, S. H.; Kim, Y. D.; Li, B.; Seo, D.; Pistunova, K.; Yin, J.; Park, J.-H.; Choi, H.-J.; Lee, Y. H.; Watanabe, K.; Taniguchi, T.; Kim, P.; Dean, C. R.; Hone, J. C. Low-Temperature Ohmic Contact to Monolayer MoS_2 by van der Waals Bonded Co/*h*−BN Electrodes. *Nano Lett.* **2017**, *17*, 4781−4786.

(21) Guan, J.; Chuang, H.-J.; Zhou, Z.; Tománek, D. Optimizing Charge Injection across Transition Metal Dichalco-genide Hetero-junctions: Theory and Experiment. *ACS Nano* **2017**, *11*, 3904−3910.

(22) Kappera, R.; Voiry, D.; Yalcin, S. E.; Branch, B.; Gupta, G.; Mohite, A. D.; Chhowalla, M. Phase-Engineered Low-resistance Contacts for Ultrathin MoS_2 Transistors. *Nat. Mater.* **2014**, *13*, 1128.

(23) Cho, S.; Kim, S.; Kim, J. H.; Zhao, J.; Seok, J.; Keum, D. H.; Baik, J.; Choe, D.-H.; Chang, K. J.; Suenaga, K.; Kim, S. W.; Lee, Y. H.; Yang, H. Phase Patterning for Ohmic Homojunction Contact in $MoTe_2$. *Science* **2015**, *349*, 625−628.

(24) Yang, H.; Kim, S. W.; Chhowalla, M.; Lee, Y. H. Structural and Quantum-State Phase Transitions in van der Waals Layered Materials. *Nat. Phys.* **2017**, *13*, 931.

(25) Heinze, S.; Tersoff, J.; Martel, R.; Derycke, V.; Appenzeller, J.; Avouris, P. Carbon Nanotubes as Schottky Barrier Transistors. *Phys. Rev. Lett.* **2002**, *89*, 106801.

(26) Yi, Y.; Wu, C.; Liu, H.; Zeng, J.; He, H.; Wang, J. A Study of Lateral Schottky Contacts in WSe_2 and MoS_2 Field Effect Transistors Using Scanning Photocurrent Microscopy. *Nanoscale* **2015**, *7*, 15711−15718.

(27) Farmanbar, M.; Brocks, G. Ohmic Contacts to 2D Semi-conductors through van der Waals Bonding. *Adv. Electr. Mater.* **2016**, *2*, 1500405.

(28) Greiner, M. T.; Helander, M. G.; Tang, W.-M.; Wang, Z.-B.; Qiu, J.; Lu, Z.-H. Universal Energy-Level Alignment of Molecules on Metal Oxides. *Nat. Mater.* **2012**, *11*, 76.

(29) Xie, L.; Wang, X.; Mao, H.; Wang, R.; Ding, M.; Wang, Y.; Özyilmaz, B.; Ping Loh, K.; Wee, A. T.; Ariando; Chen, W. Electrical Measurement of Nondestructively *p*−Type Doped Graphene Using Molybdenum Trioxide. *Appl. Phys. Lett.* **2011**, *99*, 012112.

(30) Russell, S. A.; Cao, L.; Qi, D.; Tallaire, A.; Crawford, K. G.; Wee, A. T.; Moran, D. A. Surface Transfer Doping of Diamond by MoO_3: A Combined Spectroscopic and Hall Measurement Study. *Appl. Phys. Lett.* **2013**, *103*, 202112.

(31) Chuang, S.; Battaglia, C.; Azcatl, A.; McDonnell, S.; Kang, J. S.; Yin, X.; Tosun, M.; Kapadia, R.; Fang, H.; Wallace, R. M.; Javey, A. MoS2 *p*−Type Transistors and Diodes Enabled by High Work Function MoO_x Contacts. *Nano Lett.* **2014**, *14*, 1337−1342.

(32) Xia, F.; Shao, Z.; He, Y.; Wang, R.; Wu, X.; Jiang, T.; Duhm, S.; Zhao, J.; Lee, S.-T.; Jie, J. Surface Charge Transfer Doping *via* Transition Metal Oxides for Efficient *p*−Type Doping of II−VI Nanostructures. *ACS Nano* **2016**, *10*, 10283−10293.

(33) Sivacarendran, B.; Junkai, D.; Zhen, O. J.; Sumeet, W.; James, S.; Jianshi, T.; L, W. K.; R, F. M.; Salvy, R.; Serge, Z.; S, S. M.; Nikhil, M.; Sharath, S.; Madhu, B.; Zadeh Kourosh, K. Enhanced Charge Carrier Mobility in Two-Dimensional High Dielectric Molybdenum Oxide. *Adv. Mater.* **2013**, *25*, 109−114.

(34) Ataca, C.; Şahin, H.; Ciraci, S. Stable, Single-layer MX_2 Transition-Metal Oxides and Dichalcogenides in a Honeycomb-Like Structure. *J. Phys. Chem. C* **2012**, *116*, 8983−8999.

(35) Heyd, J.; Scuseria, G. E.; Ernzerhof, M. Hybrid Functionals Based on a Screened Coulomb Potential. *J. Chem. Phys.* **2003**, *118*, 8207−8215.

(36) Krukau, A. V.; Vydrov, O. A.; Izmaylov, A. F.; Scuseria, G. E. Influence of the Exchange Screening Parameter on the Performance of Screened Hybrid Functionals. *J. Chem. Phys.* **2006**, *125*, 224106.

(37) Gong, C.; Zhang, H.; Wang, W.; Colombo, L.; Wallace, R. M.; Cho, K. Band Alignment of Two-Dimensional Transition Metal Dichalcogenides: Application in Tunnel Field Effect Transistors. *Appl. Phys. Lett.* **2013**, *103*, 053513.

(38) Li, M.-Y.; Shi, Y.; Cheng, C.-C.; Lu, L.-S.; Lin, Y.-C.; Tang, H.-L.; Tsai, M.-L.; Chu, C.-W.; Wei, K.-H.; He, J.-H.; Chang, W.-H.; Suenaga, K.; Li, L.-J. Epitaxial Growth of a Monolayer WSe_2-MoS_2 Lateral $p - n$ Junction with an Atomically Sharp Interface. *Science* **2015**, *349*, 524−528.

(39) Duan, X.; Wang, C.; Fan, Z.; Hao, G.; Kou, L.; Halim, U.; Li, H.; Wu, X.; Wang, Y.; Jiang, J.; Pan, A.; Huang, Y.; Yu, R.; Duan, X. Synthesis of $WS_{2x}Se_{2-2x}$ Alloy Nanosheets with Composition-Tunable Electronic Properties. *Nano Lett.* **2016**, *16*, 264−269.

(40) Kresse, G.; Furthmüller, J. Efficient Iterative Schemes for *Ab Initio* Total-Energy Calculations using a Plane-Wave Basis Set. *Phys. Rev. B: Condens. Matter Mater. Phys.* **1996**, *54*, 11169−11186.

(41) Kresse, G.; Furthmüller, J. Efficiency of *Ab-Initio* Total Energy Calculations for Metals and Semiconductors Using a Plane-Wave Basis Set. *Comput. Mater. Sci.* **1996**, *6*, 15−50.

(42) Kresse, G.; Hafner, J. *Ab Initio* Molecular-Dynamics Simulation of the Liquid-Metal−Amorphous-Semiconductor Transition in Germanium. *Phys. Rev. B: Condens. Matter Mater. Phys.* **1994**, *49*, 14251−14269.

(43) Blöchl, P. E. Projector Augmented-Wave Method. *Phys. Rev. B: Condens. Matter Mater. Phys.* **1994**, *50*, 17953−17979.

(44) Kresse, G.; Joubert, D. From Ultra-soft Pseudopotentials to the Projector Augmented-Wave Method. *Phys. Rev. B: Condens. Matter Mater. Phys.* **1999**, *59*, 1758−1775.

(45) Perdew, J. P.; Burke, K.; Ernzerhof, M. Generalized Gradient Approximation Made Simple. *Phys. Rev. Lett.* **1996**, *77*, 3865−3868.

(46) Klimeš, J.; Bowler, D. R.; Michaelides, A. Chemical Accuracy for the van der Waals Density Functional. *J. Phys.: Condens. Matter* **2010**, *22*, 022201.

(47) Klimeš, J.; Bowler, D. R.; Michaelides, A. Van der Waals Density Functionals Applied to Solids. *Phys. Rev. B: Condens. Matter Mater. Phys.* **2011**, *83*, 195131.

(48) Monkhorst, H. J.; Pack, J. D. Special Points for Brillouin-Zone Integrations. *Phys. Rev. B: Condens. Matter Mater. Phys.* **1976**, *13*, 5188−5192.

(49) Hestenes, M. R.; Stiefel, E. Methods of Conjugate Gradients for Solving Linear Systems. *J. Res. Natl. Bur. Stand.* **1952**, *49*, 409−436.

DOI: 10.1021/acsnano.8b08190
ACS Nano 2019, 13, 5103−5111